Turbulent kinetic energy flux and budget in a water-worked gravel bed

Ellora Padhi[1,*], *Nadia* Penna[2], *Roberto* Gaudio[2], *V. R.* Desai[1], and *Subhasish* Dey[1]

[1]Department of Civil Engineering, Indian Institute of Technology Kharagpur, Kharagpur, 721302, India
[2]Dipartimento di Ingegneria Civile, Università della Calabria, Rende, 87036, Italy

Abstract. Turbulent flow over a water-worked gravel bed (WGB) was investigated using the double-averaging methodology (DAM). The flow measurements were carried out by the particle image velocimetry (PIV) technique. The double-averaged (DA) turbulent characteristics (DA Turbulent kinetic energy (TKE) components, form-induced TKE components, DA TKE fluxes, form-induced TKE fluxes, DA TKE budget) were analyzed for the WGB. To understand the effect of changed bed topography on the turbulent characteristics, the flow measurements were carried out over a screeded gravel bed (SGB), keeping the flow Froude number same as in case of WGB. Owing to water work, the bed topography of WGB was dissimilar to that of SGB, resulting in higher roughness size for the former than that for the latter. Comparative study of the DA turbulent characteristics of both the beds infers that especially in the near-bed flow zone, the flow parameters of the WGB are attaining higher values than those of the SGB. However, they are almost alike for both the beds in the flow outer layer.

1. Introduction

Turbulent flow over a gravel bed is one of the important topics of discussion owing to its intricate behaviour in the near-bed flow zone, where the flow is vastly governed by the fluid-gravel interactions, becoming nonhomogeneous within the reach. To replicate the flow characteristics of a natural river in the laboratory, it is vital to recapture the bed condition of a natural river to ensure the accurate illustration of the riverbed. However, in the laboratory, it is very common to create the bed by placing the mixture of gravels randomly in the flume and then screeding it manually. Such a bed is quite different from the bed observed in a natural gravel-bed river. To overcome this issue, the experimental screeded gravel bed (SGB) is required to be water worked before performing the experiments, in order to get a bed surface which resembles to that of a natural gravel bed river. Such a bed is termed as water-worked gravel bed (WGB).

As bed surface topography is one of the significant parameters for analyzing the turbulence characteristics, Nikora et al. [1] conducted experimental study over both the WGB and SGB, and discovered that the roughness characteristics of both the beds are

* Corresponding author: ellora@iitkgp.ac.in

significantly different. Barison et al. [2] revealed that the near-bed spatial distribution of time-averaged velocity is different over WGB with respect to SGB owing to difference in bed roughness. The spatial patterns of time-averaged streamwise velocity in the near-bed region were investigated over WGB and the presence of spatially coherent flow structures were discovered [3, 4]. Cooper and Tait [5] found that the use of SGB underestimates the degree of temporal variability in the flow and, in addition to that, the time-averaged velocities were well organized into long streamwise flow structures over the WGB, whereas randomly organized over the SGB. Considering a flow over WGB, the level of flow spatial variability and its influence on momentum transfer were investigated [6]. A series of experiments were performed over the WGB to investigate the development of coherent secondary flow cells [7]. Later, Cooper et al. [8] revealed that the time-averaged flow over the WGB is spatially heterogeneous and strongly influenced by the relative submergence.

In spite of the several investigations on the flow over WGB, the double-averaged (DA) turbulent characteristics, especially the turbulent kinetic energy (TKE) fluxes and budget which play a dominant role in the overall structure of the near-bed flow, are still to be explored deeply. Thus, this paper provides a novel experimental study designed to contribute to such description over both the WGB and SGB by using Particle Image Velocimetry (PIV) measurements as well as to demonstrate the importance of creating WGB for simulating near-bed flow fields in laboratory model studies.

2. Experimental setup and procedure

The experiments were carried out in a recirculating rectangular 9.66 m long, 0.485 m wide tilting flume, in the Laboratory *Grandi Modelli Idraulici*, University of Calabria, Italy. For the experiment, the slope of the flume bottom was fixed with hydraulic jacks. The inlet of the flume consisted of a stilling tank, an uphill slipway and a honeycomb to reduce the pump vibrations. The flow velocity was adjusted by regulating the pump, and the flow depth (h) was controlled by an adjustable tailgate at the flume outlet. To enable visual access to the flow, the flume walls were made of glass sheets. All measurements were taken within a 1 m long stretch at a distance of 6.3 to 7.3 m from the flume inlet. The schematic of the experimental setup is shown in Fig. 1.

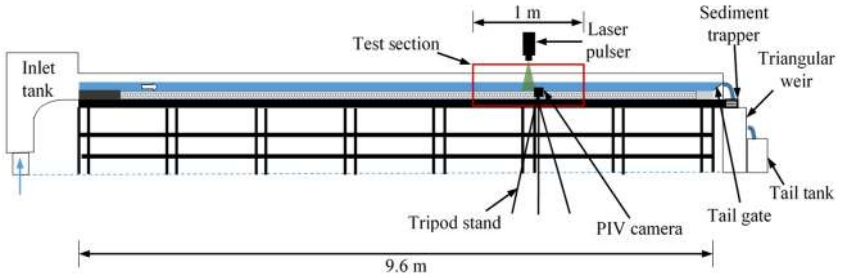

Fig. 1. Schematic of the experimental setup.

2.1. PIV measurements

For the flow field measurement a TSI® PIV system was used. It consisted of a Nikon 12-bit 2048 × 2048 px^2 CCD camera with a frame rate of 15 Hz and a double pulse Nd:YAG laser with pulse energy of 50 mJ, operated at 15 Hz with a time delay of 1000 μs between the frames. The PIV system was used at 7.25 Hz, owing to PC port frequency limitation. The flow was seeded with titanium dioxide (TiO_2) having a mean diameter of 3 μm and a density of 4.26 kg m^3. The test section was illuminated by the laser sheet to visualize the

movement of the particles that were captured by the camera placed normal to the laser sheet. For each measuring location, 3000 pairs of images were acquired, with a measuring area of 170 × 170 mm^2 (64 × 64 px^2). The image analysis provided about forty-three velocity profiles, covering an area of 120 × 100 mm^2, with a spatial resolution of 2.7 mm.

2.2. Preparation of WGB and details of flow parameters

A coarse gravel sediment mixture of size range $4 < d < 6$ mm, median diameter d_{50} of 4.81 mm and geometric standard deviation σ_g (= $(d_{84}/d_{16})^{0.5}$) of 1.18, was used as a bed material. At the first phase, the mixture was placed into the channel and screeded manually to obtain a SGB with a slope of 0. 7%. Then, the WGB was produced by a flow over a SGB that could transport the surface gravels. For the initiation of sediment motion, the average flow velocity U was considered as 0.82 m s^{-1}, which was greater than the threshold velocity for the inception of sediment motion U_c = 0.59 m s^{-1} obtained from the formula given by Neill [9]. During the preparation of the WGB, the gravel transport rate (g_s) declined from 7.2 × 10^{-2} to 3 × 10^{-4} kg m^{-1} s^{-1} in 28.5 h, as there was no gravel feeding. At the end of this phase, the bed topography was measured by the laser scanner and the bed slope S_0 was found to be 0.4%. In the second phase, the grains were placed again in the flume to recreate the earlier SGB by screeding the sediments manually, with S_0 = 0.7%. From the measurements of bed topography, the gravel crest levels were computed for the WGB and the SGB and found to be 1.96 and 2.83 mm, respectively, from the virtual bed level. The average roughness heights Δ_k for the WGB and the SGB were found to be 1.25 and 1.04 mm, respectively.

Before initiating the experiments, the U_c was again calculated by using Neill's [9] formula for h = 0.1 m, and found to be 0.60 m s^{-1}. The flow measurements were taken over the WGB and SGB for h = 0.1 m and U = 0.43 m s^{-1} < U_c, showing a clear-water condition. From the Reynolds shear stress distributions, the shear velocity u_* was obtained and found to be 0.06 and 0.08 m s^{-1} for the WGB and the SGB, respectively. The u_* was used as a scaling parameters. The flow Reynolds number R (= $4Uh/\nu$, where ν is the water kinematic viscosity = 10^{-6} m^2 s^{-1} at the temperature of 20 °C) and flow Froude number Fr (= $U/(gh)^{0.5}$, where g is the gravitational acceleration)) were determined as 1.72 × 10^5 and 0.432, respectively. The shear particle Reynolds numbers R_* (= $u_* \Delta_k / \nu$) were obtained as 78 and 85 for the WGB and the SGB, respectively. For both the cases, the values of R_* were greater than 70, confirming the occurrence of rough-turbulent flow.

3. Results and discussion

3.1. DA turbulent kinetic energy and form-induced turbulent kinetic energy

For a two-dimensional flow, the nondimensional DA TKE $\langle K^+ \rangle$ is expressed as $\langle K^+ \rangle$ = ($\langle K_u \rangle$, + $\langle K_w \rangle$) × u_*^{-2}, where $\langle K_u \rangle$ (= $0.5\langle \overline{u'u'} \rangle$, u' being the streamwise temporal velocity fluctuation), and $\langle K_w \rangle$ (= $0.5\langle \overline{w'w'} \rangle$, w' being the vertical temporal velocity fluctuation), are the nondimensional streamwise and vertical TKE components, respectively [10]. For both the WGB and SGB, the variations of $\langle K_u \rangle$ and $\langle K_w \rangle$ with $\tilde{z}$ are shown in Figs. 2(a) and 2(b), respectively. It is observed that for both the beds, the magnitudes of $\langle K_u \rangle$ increase with an increase in $\tilde{z}$ and attain their respective peaks above the crest level. Then, they decrease with a further increase in $\tilde{z}$. Similar observations were found in the case of $\langle K_w \rangle$ profiles for both the beds. This suggests that in the near-bed flow region, the mixing process in the presence of roughness elements increases the turbulence level, and as a result, u' and w' get enhanced. However, the effect of mixing gradually decreases above the form-induced

sublayer, resulting in reduced values of TKE components [10–13]. The variations of $\langle K^+ \rangle$ with $\tilde{z}$ for the WGB and SGB are shown in Fig. 2(c). As expected, the $\langle K^+ \rangle$ attain their peaks above the crest level, then decrease with an increase in $\tilde{z}$. This happens owing to the reduction in u' and w' values. Further, comparative study infers that for the WGB, the $\langle K_u \rangle$, $\langle K_w \rangle$ and $\langle K^+ \rangle$ attain higher values than those for the SGB owing to higher bed roughness of the former than that of the latter [14].

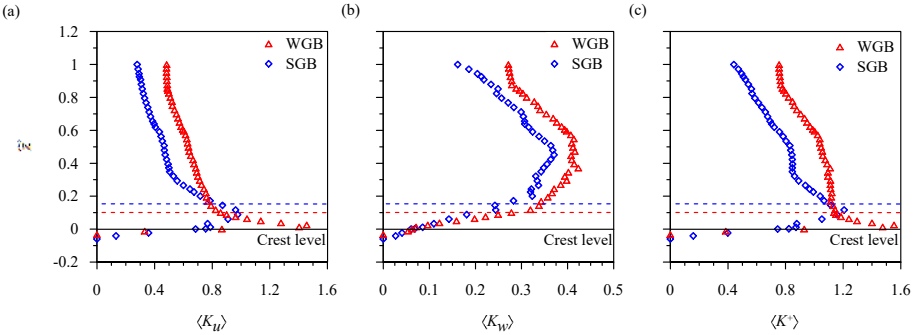

Fig. 2. (a) Variations of nondimensional DA streamwise component $\langle K_u \rangle$ with nondimensional vertical distance $\tilde{z}$ over the WGB and SGB, (b) variations of nondimensional DA vertical component $\langle K_w \rangle$ with $\tilde{z}$ over the WGB and SGB and (c) variations of total nondimensional DA TKE $\langle K^+ \rangle$ with $\tilde{z}$ over the WGB and SGB.

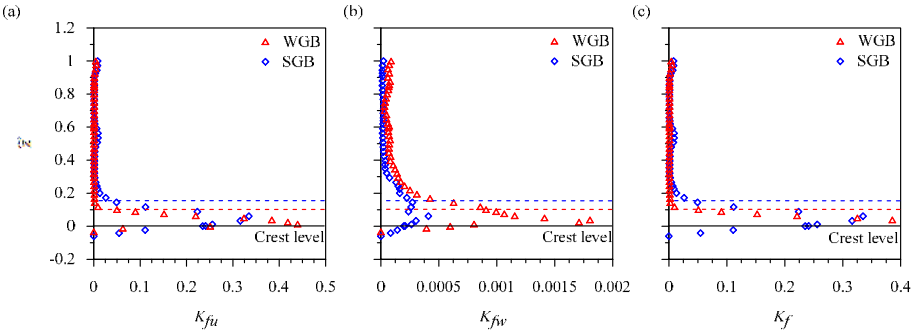

Fig. 3. (a) Variations of nondimensional form-induced streamwise component $\langle K_{fu} \rangle$ with nondimensional vertical distance $\tilde{z}$ over the WGB and SGB, (b) variations of nondimensional form-induced vertical component $\langle K_{fw} \rangle$ with $\tilde{z}$ over the WGB and SGB and (c) variations of nondimensional form-induced total TKE $\langle K_f \rangle$ with $\tilde{z}$ over the WGB and SGB.

Similarly, the nondimensional form-induced TKE $\langle K_f \rangle$ expressed as $\langle K_f \rangle = (\langle K_{fu} \rangle, + \langle K_{fw} \rangle) \times u_*^{-2}$, where $\langle K_{fu} \rangle$ (= $0.5\langle \tilde{u}\tilde{u} \rangle$, $\tilde{u}$ being the streamwise spatial velocity fluctuation), and $\langle K_{fw} \rangle$ (= $0.5\langle \tilde{w}\tilde{w} \rangle$, $\tilde{w}$ being the vertical spatial velocity fluctuation), are the nondimensional streamwise and vertical form-induced TKE components, respectively [10]. Figures 3(a–c) show the variations of $\langle K_{fu} \rangle$, $\langle K_{fw} \rangle$ and $\langle K_f \rangle$ with $\tilde{z}$ for the WGB and SGB. The $\langle K_{fu} \rangle$ start growing at $\tilde{z}$ = 0.1 and $\tilde{z}$ = 0.14 for the WGB and SGB, respectively. They attain their peaks above the crest level, decreasing afterward with a decrease in $\tilde{z}$ for both the beds (Fig. 3(a)). Like $\langle K_{fu} \rangle$, the profiles of $\langle K_{fw} \rangle$ and $\langle K_f \rangle$ also follow the similar trend, attain their peaks above the crest level, and get diminished with a decrease in $\tilde{z}$ for both the beds. It suggests that within the form-induced sublayer, the $\langle K_{fu} \rangle$, $\langle K_{fu} \rangle$ and $\langle K_f \rangle$ increase owing to an increase in $\tilde{u}$ and $\tilde{w}$, whereas within the interfacial sublayer, a reduction in $\tilde{u}$ and $\tilde{w}$ results in a decrease in $\langle K_{fu} \rangle$, $\langle K_{fu} \rangle$ and $\langle K_f \rangle$ [11,13]. From Figs. 3(a-c), it is observed

that the magnitude of $\langle K_{fu} \rangle$, $\langle K_{fw} \rangle$ and $\langle K_f \rangle$ are found to be higher for WGB than those for SGB owing to the difference in spatial orientation of the roughness elements of the beds.

3.2. DA turbulent kinetic energy fluxes and form- induced turbulent kinetic energy fluxes

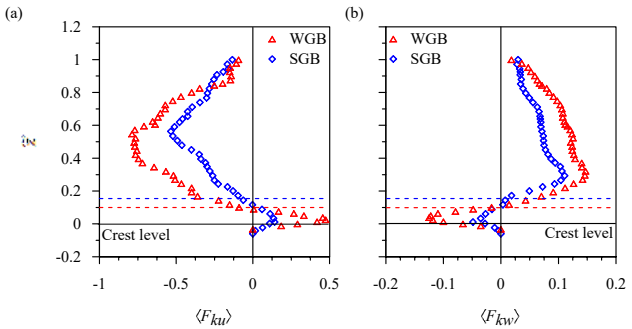

Fig. 4. (a) Variations of nondimensional DA streamwise TKE flux $\langle F_{ku} \rangle$ with nondimensional vertical distance $\tilde{z}$ over the WGB and SGB and (b) variations of nondimensional DA vertical TKE flux $\langle F_{kw} \rangle$ with nondimensional vertical distance $\tilde{z}$ over the WGB and SGB.

The nondimensional DA streamwise and vertical TKE fluxes are represented as $(\langle F_{ku} \rangle, (\langle F_{kw} \rangle) = (\langle f_{ku} \rangle, \langle f_{kw} \rangle) \times u_*^{-3}$, respectively. The flow in the present study is considered to be two-dimensional, therefore, DA streamwise TKE flux $f_{ku} = 0.75(\overline{u'u'u' + u'w'w'})$ and DA vertical TKE flux $f_{kw} = 0.75(\overline{u'u'w' + w'w'w'})$ [15]. For both the WGB and SGB, the variations of $\langle F_{ku} \rangle$ with $\tilde{z}$ are shown in Fig. 4(a). The $\langle F_{ku} \rangle$ start with the positive values, attaining their peaks above the crest level; thereafter, their magnitudes start diminishing with a further increase in $\tilde{z}$. At $\tilde{z} = 0.1$ (for WGB) and 0.12 (for SGB), the $\langle F_{ku} \rangle$ become negative, and continued to be the same for the remaining flow depth. The positive sign infers that the $\langle F_{ku} \rangle$ transports in the downstream direction, whereas the negative sign suggests that the $\langle F_{ku} \rangle$ transports in the upstream direction [10, 12, 15, 16]. Fig. 4(a) suggests that the magnitude of $\langle F_{ku} \rangle$ for the WGB is higher than that for the SGB, which is attributed to high temporal velocity fluctuations for the former.

Referring to Fig. 4(b), the $\langle F_{kw} \rangle$ for the WGB and SGB initiate with small negative values, attaining their respective negative peaks at $\tilde{z} = 0.025$ and 0. Thereafter, they start diminishing with an increase in $\tilde{z}$, becoming positive at $\tilde{z} = 0.1$ and 0.12 for the WGB and SGB, respectively. The negative sign signifies a downward transport of $\langle F_{kw} \rangle$, whereas the positive sign indicates an upward transport of $\langle F_{kw} \rangle$ [10, 11, 15, 16]. Comparative study suggests that for a given $\tilde{z}$, the value of $\langle F_{kw} \rangle$ for the WGB is larger than that for the SGB and the reason behind this is the same as stated earlier for the $\langle F_{ku} \rangle$ profiles.

The profiles of $\langle F_{ku} \rangle$ and $\langle F_{kw} \rangle$ provide information about the bursting events. For $\langle F_{ku} \rangle > 0$ and $\langle F_{kw} \rangle < 0$, result in sweeps; while for $\langle F_{ku} \rangle < 0$ and $\langle F_{kw} \rangle > 0$, result in ejections [10, 11]. This infers that the sweeps are the dominating events up to $\tilde{z} = 0.1$ and 0.12 for the WGB and SGB, respectively (Fig. 6(a)), while the ejections become the governing mechanism for $\tilde{z} > 0.1$ and 0.12 for the former and the latter, respectively (Fig. 4(b)).

The nondimensional streamwise and vertical form-induced TKE fluxes are calculated as $(\langle F_{fu} \rangle, \langle F_{fw} \rangle) = (0.75(\langle \tilde{u}\tilde{u}\tilde{u} \rangle + \langle \tilde{u}\tilde{w}\tilde{w} \rangle), 0.75(\langle \tilde{u}\tilde{u}\tilde{w} \rangle + \langle \tilde{w}\tilde{w}\tilde{w} \rangle)) \times u_*^{-3}$, respectively. For the WGB and SGB, the variations of $\langle F_{fu} \rangle$ with $\tilde{z}$ are shown in Fig. 5(a). For both the beds, the $\langle F_{fu} \rangle$ start with positive values increasing gradually with an increase in $\tilde{z}$. For the WGB,

the $\langle F_{fu} \rangle$ attains its positive peak above the crest level ($\tilde{z}$ = 0.0025), whereas, for the SGB, the peak appears at $\tilde{z}$ = 0.01. Thereafter, they tend to decline with an increase in $\tilde{z}$. For these cases, the $\langle F_{fu} \rangle$ almost vanish above the form-induced sublayer.

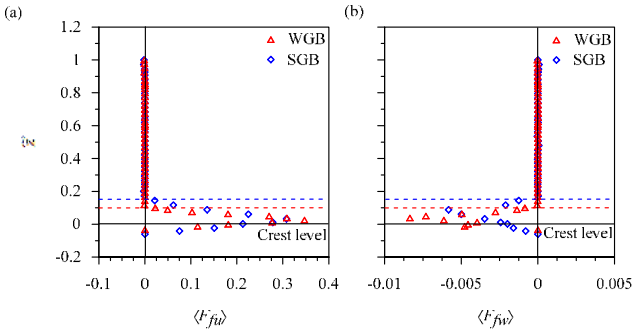

Fig. 5. (a) Variations of dimensionless DA streamwise TKE flux $\langle F_{fu} \rangle$ with non-dimensional vertical distance $\tilde{z}$ over the WGB and SGB and (b) variations of dimensionless DA vertical TKE flux $\langle F_{fw} \rangle$ with dimensionless vertical distance $\tilde{z}$ over the WGB and SGB.

The $\langle F_{fw} \rangle$ profiles for both the beds start growing with negative values with an increase in $\tilde{z}$ (Figs. 5(b)). The $\langle F_{fw} \rangle$ attain their respective negative peak values above the crest level for both the cases. After achieving the peak, their values start diminishing with an increase in $\tilde{z}$, becoming negligible above the form-induced sublayer. It is noticeable that $\tilde{w}$ is quite less than $\tilde{u}$, resulting in a far smaller value of $\langle F_{fw} \rangle$ than $\langle F_{fu} \rangle$. Comparative study infers that the magnitude of $\langle F_{fw} \rangle$ for the WGB is higher than that for the SGB.

3.3. DA Turbulent kinetic energy budget

The DA TKE budget equation for a gravel-bed open-channel flow can be expressed as follows:

$$\underbrace{\langle \overline{u'w'} \rangle \frac{\partial \langle \overline{u} \rangle}{\partial z}}_{\langle t_P \rangle} = \langle \varepsilon \rangle + \underbrace{\frac{\partial \langle f_{kw} \rangle}{\partial z}}_{\langle t_D \rangle} + \underbrace{\frac{\partial \langle f_{fw} \rangle}{\partial z}}_{\langle t_F \rangle} + \underbrace{\frac{1}{\rho} \frac{\partial \langle \overline{p'w'} \rangle}{\partial z}}_{\langle p_D \rangle} - \underbrace{\nu \frac{\partial^2 \langle k \rangle}{\partial z^2}}_{\langle \nu_D \rangle}, \quad (1)$$

where t_P is the TKE production rate, ε is the dissipation rate, t_D is the TKE diffusion rate, t_F is the form-induced diffusion rate, p_D is the pressure energy diffusion, ν_D is the viscous diffusion and p' is the pressure fluctuations. The effect of viscous diffusion rate $\langle \nu_D \rangle$ is negligible because of the large value of R. Except the $\langle p_D \rangle$, all the parameters in Eq. (1) are determined experimentally. Thus, p_D is estimated as $p_D = t_P - \varepsilon - t_D - t_F$. All the DA TKE budget components are made nondimensional by multiplying h / U^3 and represented as $\langle T_P \rangle$, $\langle E_D \rangle$, $\langle T_D \rangle$, $\langle T_F \rangle$, $\langle P_D \rangle$. Figures 6(a–e) show the variations of $\langle T_P \rangle$, $\langle E_D \rangle$, $\langle T_D \rangle$, $\langle T_F \rangle$, and $\langle P_D \rangle$ with $\tilde{z}$ for the WGB and SGB, respectively.

The $\langle T_P \rangle$ develop below the crest level, increasing rapidly with $\tilde{z}$ within the respective form-induced sublayers for the WGB and SGB (Fig. 6(a)). The $\langle T_P \rangle$ of both the beds attain their peaks near the outer edge of their form-induced sublayers, then start to diminish towards the free surface. For $\tilde{z} < 0.1$, the value of $\langle T_P \rangle$ for WGB is greater than that for the SGB, but for $\tilde{z} \geq 0.1$, the value of $\langle T_P \rangle$ for the latter becomes greater than that for the former. It infers that for $\tilde{z} < 0.1$, the effects of the change in bed roughness are stronger, resulting in a larger value of $\langle T_P \rangle$ for the WGB than that for the SGB. However, for $\tilde{z} >$

0.1, the effects get diminished, triggering the $\langle T_P \rangle$ to be larger for the SGB than that for the WGB.

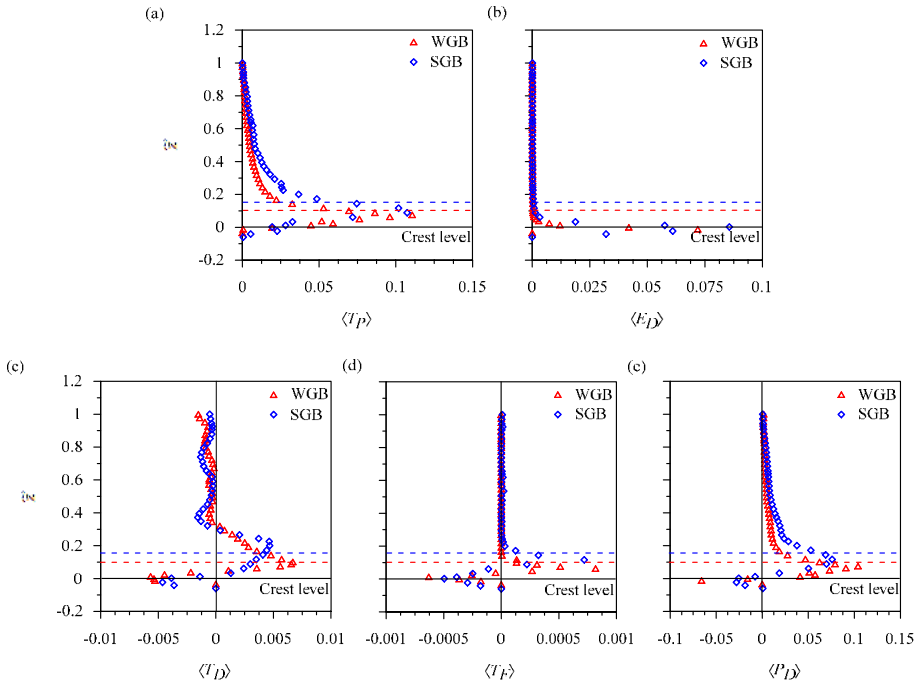

Fig. 6. Variations of dimensionless (a) DA TKE production rate $\langle T_P \rangle$, (b) DA TKE dissipation rate $\langle E_D \rangle$, (c) DA TKE diffusion rate $\langle T_D \rangle$, (d) form-induced diffusion rate $\langle T_F \rangle$ and (e) DA pressure energy diffusion rate $\langle P_D \rangle$ with dimensionless vertical distance $\tilde{z}$ over the WGB and SGB.

Considering the formula given by Krogstad and Antonia [17], the DA $\langle \varepsilon \rangle$ can be determined as $\langle \varepsilon \rangle = (15\nu \langle \overline{\partial u' / \partial t} \rangle) \times \langle \bar{u} \rangle^{-2}$, where $\langle \bar{u} \rangle$ is the DA streamwise velocity. For the WGB and SGB, the variations of $\langle E_D \rangle$ with $\tilde{z}$ are presented in Fig. 6(b). The $\langle E_D \rangle$ increase rapidly below the crest level, reaching their peak just near the crest level. Importantly, the $\langle E_D \rangle$ for the SGB is found to be larger than that for the WGB and the reason behind this is attributed to the larger value of $\langle \bar{u} \rangle$ for the former than that for the latter.

Variations of the $\langle T_D \rangle$ with $\tilde{z}$ for the WGB and SGB are shown in Fig. 6(c). The $\langle T_D \rangle$ profiles develop with negative values, increasing rapidly with $\tilde{z}$ for both the beds. The negative peak values of $\langle T_D \rangle$ appear at $\tilde{z}$ = 0.01 and –0.002 for the WGB and SGB, respectively. Subsequently, the $\langle T_D \rangle$ for both the beds increase with an increase in $\tilde{z}$, becoming positive at $\tilde{z}$ = 0.064 and 0.025, respectively. However, after achieving their positive peaks, they tend to decrease, becoming negative at $\tilde{z}$ = 0.35 and 0.3 for the WGB and SGB, respectively. The difference in the magnitude of $\langle T_D \rangle$ obtained for the WGB and SGB is caused by the difference in temporal velocity fluctuations induced by the two beds.

Further, the magnitudes of $\langle T_F \rangle$ are fairly negligible as compared to that of $\langle T_D \rangle$ for both the WGB and SGB (Fig. 6(d)). Like the $\langle T_D \rangle$, the $\langle T_F \rangle$ start with very small negative values, attaining their negative peaks just near the crest level for both the cases. Afterword, they increase with an increase in $\tilde{z}$, changing their sign to become positive at $\tilde{z}$ = 0.05 and 0.075 for the WGB and SGB, respectively. After reaching their respective positive peaks, the magnitudes of $\langle T_F \rangle$ tend to decline with an increase in $\tilde{z}$, becoming vanishingly small above the corresponding form-induced sublayer, for both WGB and SGB.

Figure 6(e) shows the variations of $\langle P_D \rangle$ with $\tilde{z}$ for the WGB and SGB. It is evident that the $\langle P_D \rangle$ begin with negative values, attaining their negative peaks below the crest level for both the beds. Then, they decrease sharply, becoming positive above the crest level for both the cases. For the WGB, the $\langle P_D \rangle$ reaches its positive peak at $\tilde{z}$ = 0.075, while for the SGB, the positive peak occurs at $\tilde{z}$ = 0.1. However, they tend to decline afterwards with an increase in $\tilde{z}$. The negative sign of $\langle P_D \rangle$ indicates a gain in TKE production [11, 12]. The $\langle P_D \rangle$ for the WGB attains a greater value than that for the SGB in the near-bed flow zone. The reason is attributed to the difference in bed topography of both the beds.

4. Conclusions

Experimental studies were carried out in order to explore the difference in turbulence characteristics between the WGB and SGB by keeping same flow condition. Owing to water work, the bed topography of WGB was dissimilar to that of SGB, resulting in higher roughness size for the former than that for the latter. The DA TKE components are small in the near-bed flow zone and grow with an increase in vertical distance for the WGB and SGB as well. Owing to higher temporal velocity fluctuations for the WGB, the DA TKE components for the WGB attain greater values than those for the SGB. The DA TKE fluxes for the WGB and SGB change their signs above the crest level, showing the changeover of the dominance of the bursting events, although in the near-bed flow zone, a significant difference in magnitude of the DA TKE fluxes is observed between the WGB and SGB. Comparative study shows that all the DA TKE budget parameters except the dissipation rate term for the WGB attain higher magnitudes than those for the SGB in the near-bed flow zone. This study reveals that the SGB causes an underestimation of turbulence parameters in comparison to WGB. Hence, it is prudent to perform experimental study over a WGB.

References

1. V. I. Nikora, D. G. Goring, B. J. F. Biggs, Water Resour. Res. **34**, 517–527 (1998)
2. S. Barison, A. Chegini, A. Marion, S.J. Tait, *Proceedings of XXX IAHR Congress*, Thessalonki, Greece, 509-516 (2003)
3. J. R. Cooper, S. J. Tait, Acta Geophys. **56**, 614–641 (2008)
4. R. J. Hardy, J. L. Best, S. N. Lane, P. E. Carbonneau, J. Geophys. Res. **114**, F01003 (2009)
5. J. R. Cooper, S. J. Tait, Earth Surf. Process. Landf. **34**, 384–397 (2009)
6. J. R. Cooper, S. J. Tait, Water Resour. Res. **46,** W11559 (2010)
7. S. J. Mclelland, in *Coherent Flow Structures at Earth's Surface* (Chichester, 2013)
8. J. R. Cooper, J. Aberle, K. Koll, S. J. Tait, Water Resour. Res. **49**, 5765–5777 (2013)
9. C. R. Neill, *Proceedings of XII IAHR Congress*, Fort Collins, Colorado, **1**, 46–54 (1967)
10. S. Sarkar, A. N. Papanicolao, S. Dey, J. Hydraul. Eng. **142**, 04016052 (2016)
11. S. Dey, R. Das, J. Hydraul Eng. **138**, 707–725 (2012)
12. C. Manes, D. Pokrajac, I. Mcewan, J. Hydraul. Eng. **133**, 896–904 (2007)
13. D. Ferraro, S. Servidio, V. Carbone, S. Dey, R. Gaudio, J. Fluid Mech. **798**, 540–571 (2016)
14. I. Nezu, H. Nakagawa, *Turbulence in Open-Channel Flows* (Rotterdam, 1993)
15. S. Dey, *Fluvial Hydrodynamics: Hydrodynamic and Sediment Transport Phenomena* (Springer-Verlag, Berlin, 2014)
16. E. Mignot, E. Barthelemy, and D. Hurther, J. Fluid Mech. **618**, 279–303 (2009).
17. P. A. Krogstad, R.A. Antonia, Exp. Fluids **27**, 450–460 (1999)